nature electronics

Article

https://doi.org/10.1038/s41928-025-01434-x

A 64-kilobit spin–orbit torque magnetic random-access memory based on back-end-of-line-compatible β-tungsten

Received: 9 May 2024

Accepted: 10 July 2025

Published online: 02 September 2025

Check for updates

Yen-Lin Huang[1] ✉, MingYuan Song[2], Chien-Min Lee[2], Yu-Wei Chen[1], Ching-Yu Chiang[3], Shih-Hsiang Chou[1], Liang-Chao Hsu[1], Heng-Jui Liu[4], Guan-Long Chen[5], Shan-Yi Yang[5], Yao-Jen Chang[5], I-Jung Wang[5], Yu-Chen Hsin[5], Yi-Hui Su[5], Jeng-Hua Wei[5], Fen Xue[6], Shan X. Wang[6,7] & Xinyu Bao[2]

Magnetization switching driven by spin–orbit torque could be used to create an energy-efficient form of magnetic random-access memory. Tungsten is a promising heavy metal for such applications and can generate large spin–orbit torques when stabilized in its β-phase. However, the α-phase, which has a lower spin-Hall angle, is more thermodynamically stable. It is thus challenging to integrate metastable β-tungsten into complementary metal–oxide–semiconductor processes while maintaining phase stability under the back-end-of-line thermal constraints (400 °C for extended durations). Here we show that the insertion of thin layers of cobalt can be used to stabilize β-tungsten under back-end-of-line-compatible thermal conditions. Our composite β-tungsten layers can maintain their phase up to 400 °C for 10 h and can withstand 700 °C for 30 min. The film stacks exhibit a spin-Hall conductivity of around 4,500 Ω^{-1} cm^{-1}, which we measure by means of spin-torque ferromagnetic resonance and harmonic Hall resistance measurements. Using the tungsten composite film stacks, we fabricate a 64-kb spin–orbit torque magnetic random-access memory that offers a spin–orbit torque switching of 1 ns, data retention of more than 10 years and a tunnelling magnetoresistance of 146%.

Computing systems rely on memory subsystems that include static random-access memory, dynamic random-access memory and Flash memory. These charge-based memories face scalability challenges beyond the 10-nm node, which will affect performance, reliability and read/write disturbances[1,2]. Emerging non-volatile memory technology, such as spin–orbit torque magnetic random-access memory (SOT-MRAM), spin-transfer torque magnetic random-access memory (STT-MRAM), phase change memory[3], resistive random-access memory[4] and ferroelectric random-access memory[5,6], are non-volatile, have low latency, low power consumption and can be integrated with complementary metal–oxide–semiconductor (CMOS) technology[7–15]. They could thus be used to develop new computing architectures.

SOT-MRAM could replace cache-level static random-access memory because of its fast write speed, high energy efficiency and reliability[16–20]. SOT-MRAM uses spin–orbit torque (SOT) generated from materials with strong spin–orbit coupling to switch the magnetization

[1]Department of Materials Science and Engineering, National Yang Ming Chiao Tung University, Hsinchu, Taiwan. [2]Corporate Research, Taiwan Semiconductor Manufacturing Company, Hsinchu, Taiwan. [3]National Synchrotron Radiation Research Center, Hsinchu, Taiwan. [4]Department of Materials Science and Engineering, National Chung Hsing University, Taichung, Taiwan. [5]Electronic and Optoelectronic System Research Laboratories, Industrial Technology Research Institute, Hsinchu, Taiwan. [6]Department of Materials Science and Engineering, Stanford University, Stanford, CA, USA. [7]Department of Electrical Engineering, Stanford University, Stanford, CA, USA. ✉e-mail: yenlinhuang@nycu.edu.tw

https://doi.org/10.1038/s41928-025-01434-x

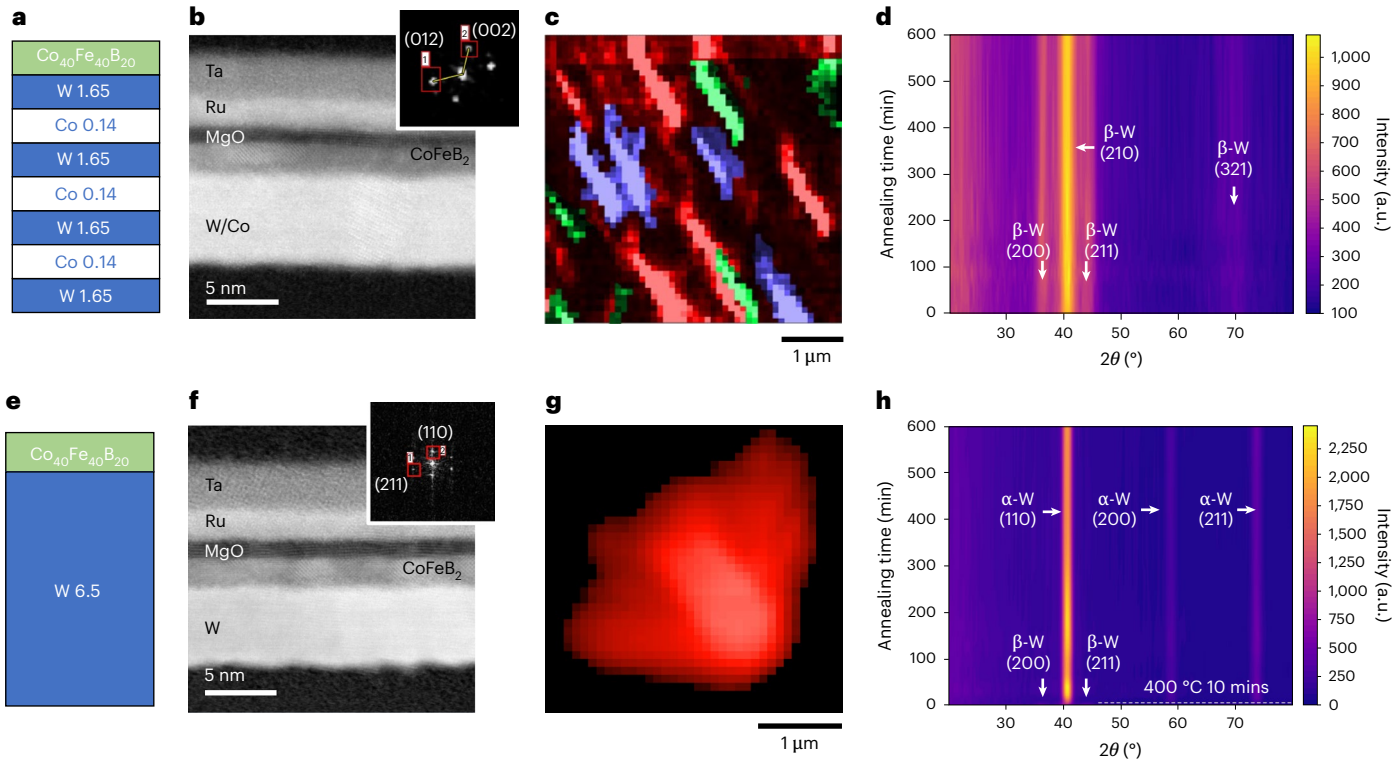

Fig. 1 | Structure and phase characterization of composite-W and single-layer-W films. a, Schematic of composite-W film structure, incorporating a three-layer 0.14-nm Co insertion (numbers show layer thickness in nanometres). The free layer consists of 2-nm $Co_{40}Fe_{40}B_{20}$, with a total nominal W thickness of 6.6 nm. **b**, Cross-sectional scanning transmission electron microscopy image of the composite-W film, capped with a Ta/Ru/MgO layer. The inset shows the electron diffraction pattern confirming the β-W phase through identification of the (002) and (012) reflections in reciprocal space. **c**, X-ray nanodiffraction mapping of the β-W phase. The contributions from the (400), (420) and (431) planes are shown in red, blue and green, respectively. The stripy crystal features align with the direction of the annealing field direction. **d**, GIXRD patterns showing the annealing time dependence of the composite-W film. **e**, Single-layer-W film schematic with a nominal thickness of 6.5 nm (numbers show layer thickness in nanometres). The free layer is 2-nm $Co_{40}Fe_{40}B_{20}$. **f**, Cross-sectional scanning transmission electron microscopy image of the single-layer-W film with the same capping layer. The inset shows the electron diffraction pattern confirming the α-W phase, identified through the (110) and (211) reflections in reciprocal space. **g**, X-ray nanodiffraction mapping of the α-W phase (400) plane for the single-layer-W case. **h**, GIXRD patterns showing the annealing time dependence for the single-layer-W film.

direction of nanomagnets within magnetic tunnel junctions (MTJs). Furthermore, three-terminal SOT-MRAM, which offers a distinct separation of write and read current paths, can address issues such as endurance and resistance limits of MTJs, that are associated with STT-MRAM[21].

When selecting spin–orbit coupling materials for SOT-MRAM, tungsten (W) is a good candidate owing to its strong spin–orbit coupling. In particular, W stabilized in the A15 structure (β-phase) can exhibit spin-Hall angles ranging from around −0.4 to −0.6 and thus has an excellent SOT efficiency[22–25]. However, β-W is a metastable phase that transforms to the thermodynamically stable α-W phase when the film thickness exceeds 4–5 nm or during the back-end-of-line (BEOL) metallization annealing (typically requiring 400 °C for up to several hours)[22]. This transformation reduces performance, as α-W has a much lower spin-Hall angle of around −0.01, resulting in less efficient SOT switching. Furthermore, the thickness of the W layer is a critical factor in the MTJ formation process. A sufficiently thick W layer is needed to prevent the etching process window from becoming too narrow, ensuring better process control and yield. However, increasing the thickness of W also raises the risk of phase transformation[26].

In this Article, we report a cobalt (Co) insertion layer design that can stabilize the β-W phase under BEOL-compatible annealing conditions. The approach allows thick W layers to be created without compromising thermal stability or spin-Hall conductivity. Our β-W films have a spin-Hall conductivity of approximately 4,500 Ω^{-1} cm^{-1}, measured by means of spin-torque ferromagnetic resonance (ST-FMR) and harmonic Hall resistance measurements. Furthermore, we use the composite-W film stack to create a 64-kb SOT-MRAM that exhibits 1-ns SOT switching, data retention of more than 10 years and 146% tunnelling magnetoresistance.

Thermodynamically stable W layer

To enhance the thermal stability of β-W, we introduced multiple Co diffusion barrier layers to suppress diffusion and mitigate phase transformation within the W layer (Fig. 1). Figure 1a,e illustrates the 6.5-nm single-layer W sample with film stack sequenced from the substrate to top as Si/SiO_2/W(6.6)/$Co_{40}Fe_{40}B_{20}$(2.0)/MgO(1.5)/Ru(2.0)/Ta(3.0) (the numbers inside parenthesis refer to thicknesses in units of nanometres) and the 6.6-nm composite-W sample with film stack sequenced as Si/SiO_2/W(1.65)/Co(0.14)/W(1.65)/Co(0.14)/W(1.65)/Co(0.14)/W(1.65)/$Co_{40}Fe_{40}B_{20}$(2.0)/MgO(1.5)/Ru(2.0)/Ta(3.0). All samples were annealed in a high vacuum of around 10^{-6} Torr at 400 °C for 30 min with a 1-T in-plane magnetic field. Under this thermal treatment, both the single-layer W and the composite-W samples show a highly crystallized structure revealed by cross-section transmission electron microscopy (TEM) images and X-ray diffraction patterns as shown in Fig. 1b–d,f–h. For the composite-W sample, we identified β-W by extracting the corresponding lattice constants (002) and (012), diffraction spots and diffraction pattern from the TEM image in Fig. 1b. The α-W lattice constants were extracted from the (110) and (211) diffraction spots in Fig. 1f. TEM analysis revealed that the 6.5-nm single-layer W sample underwent a complete phase transformation

https://doi.org/10.1038/s41928-025-01434-x

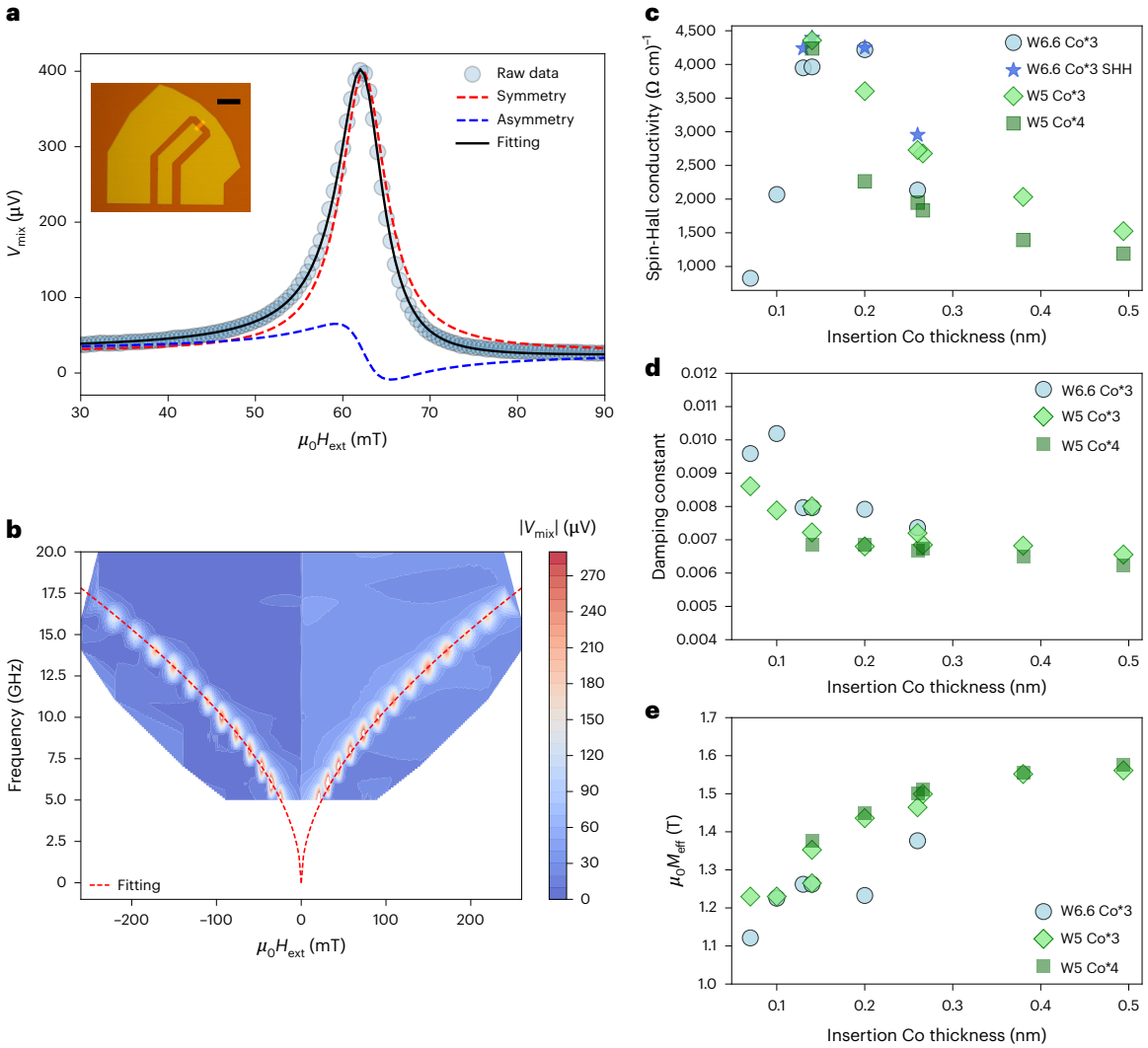

Fig. 2 | ST-FMR and harmonic Hall measurements of the SOTs in the composite-W structures. a, Typical ST-FMR spectrum for the 6.6-nm composite-W sample measured in sweeping-field mode at 8 GHz. The measured V_{mix} (raw data) is displayed alongside the fitted, symmetric and asymmetric Lorentzian functions represented in black, red and blue, respectively. The inset shows the ST-FMR device with dimensions of 10 μm × 40 μm. Inset scale bar, 100 μm. **b**, ST-FMR spectra for the 6.6-nm composite-W sample measured in sweeping-field mode with frequencies ranging from 5 to 20 GHz. The correlation of FMR resonant frequency as a function of magnetic field is used in the Kittel formula fitting (red dashed lines). **c**, Dependence of spin-Hall conductivity on Co insertion layer thickness measured on three samples: a 6.6-nm composite-W with three layers of Co insertion where the spin-Hall conductivity was extracted from the harmonic Hall measurements (W6.6 Co*3 (SHH)), a 5-nm composite-W with three layers of Co insertion (W5 Co*3) and 5-nm composite-W with four layers of Co insertion (W5 Co*4). **d**, Dependence of damping constant on the insertion Co thickness. **e**, Dependence of effective diamagnetic field ($\mu_0 M_{eff}$) on insertion Co thickness.

into the thermodynamically stable α-W, emphasizing the instability of β-W in the absence of an insertion layer.

To investigate the W phase distribution at a larger scale, nanodiffraction mappings were performed at the Taiwan Photon Source beamline 21 A. Monochromatic X-rays, selected based on the lattice constants of α-W or β-W, were used across a scan area of around 5 μm × 5 μm. Figure 1c shows stripy, crystallized β-W, aligned along the annealing field direction, induced by the insertion of a magnetic Co layer under a 1-T annealing field. Conversely, Fig. 1g shows the single-layer-W sample with homogeneously distributed α-W diffraction signals, consistent with the results obtained with TEM and grazing incidence X-ray diffraction (GIXRD) (Fig. 1h and Supplementary Fig. 1). We note that the dark areas in the nanodiffraction mappings indicate a deficiency of diffraction intensity under selected Bragg conditions. Moreover, we examined the thermal stability of composite-W by annealing it at 400 °C for up to 10 h and 700 °C for 30 min. The composite-W retained the β-W diffraction pattern (Fig. 1d and Supplementary Fig. 1). By contrast, the single-layer W underwent a phase transformation after just 10 min at 400 °C (Fig. 1h and Supplementary Fig. 1). These results show that the β-W phase in the composite-W structure is more thermally stable compared with conventional single-layer W.

The insertion of a (para)magnetic Co layer serves as an effective diffusion barrier, preventing the diffusion-induced phase transformation from β-W to α-W. Our approach demonstrates resilience to the BEOL thermal budget while preserving the spin-Hall conductivity of β-W. Moreover, the distinctive design of the stripy crystallized composite-W seems to introduce a symmetry-breaking effect (Supplementary Information Note 1), potentially enhancing the field-free SOT switching.

Spin-torque ferromagnetic resonance characterization

We measured ST-FMR on micro-sized single-layer W and composite-W samples to determine their effective spin-Hall angle θ_{SH}, effective

https://doi.org/10.1038/s41928-025-01434-x

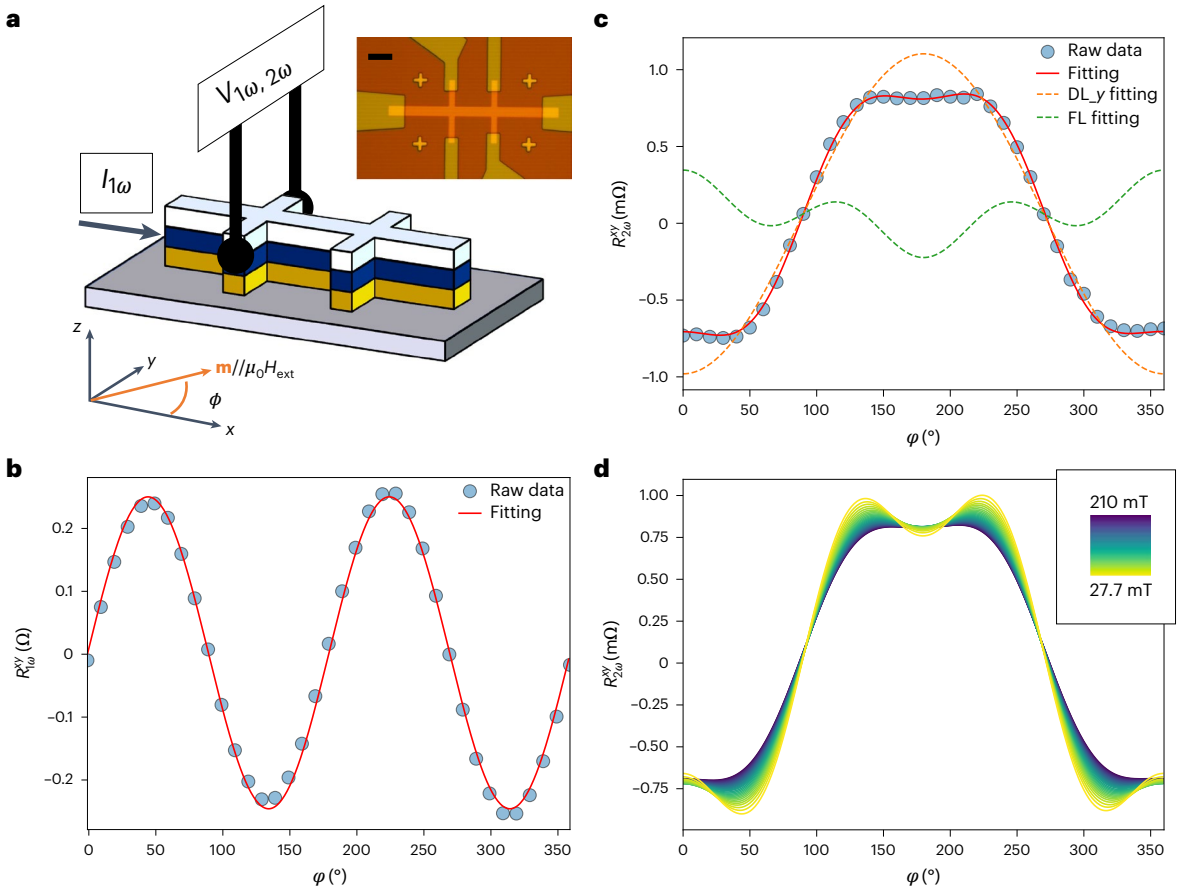

Fig. 3 | Harmonic Hall measurements of SOTs in the composite-W structures. **a**, Hall-bar measurement geometry schematic, accompanied by the definition of coordinates employed in the harmonic Hall-voltage measurements used to quantify the SOT in our samples. The angle ∅ is denoted as the angle between current direction ($I_{1\omega}$) and the applied field ($\mu_0 H_{ext}$). Inset scale bar, 20 μm. **b**, First-harmonic Hall resistance $R^{xy}_{1\omega}$ (blue dots are raw data) plotted against the in-plane magnetic field rotation angle φ (210 mT) for the 6.6-nm composite-W sample (the solid, red line shows fit to the data). **c**, Second-harmonic Hall resistance $R^{xy}_{2\omega}$ (blue dots raw data) shows in-plane rotation angle φ dependence under the application of a magnetic field of 210 mT for the 6.6-nm composite-W sample. The solid red line is the fit to the data, the dashed red line (DL_*y* fitting) and dashed green line (FL fitting) are damping-like and field-like contributions, respectively. **d**, Second-harmonic Hall resistance $R^{xy}_{2\omega}$ as a function of the in-plane magnetic field rotation angle ∅ under the application of an external magnetic field ranging from 27.7 mT to 210 mT for the 6.6-nm composite-W sample.

demagnetization field $\mu_0 M_{eff}$ and Gilbert damping constant α. The inset of Fig. 2a shows an optical microscope image of our typical ST-FMR test device with a 45° applied external magnetic field $\mu_0 H_{ext}$. The device dimensions were 60 μm × 20 μm (Fig. 2a). During the ST-FMR measurements, an in-plane alternating radiofrequency (RF) current I_{RF} was sent through the device, which generated spin–orbit torques as well as an Oersted field exerted on the magnetic moment in the adjacent $Co_{40}Fe_{40}B_{20}$ layer. When the frequency f of I_{RF} and the magnitude of the $\mu_0 H_{ext}$ satisfy the ferromagnetic resonance condition, the magnetic moment precession described by the Kittel formula in SI units $f = (\gamma/2\pi)\sqrt{\mu_0 H_0(\mu_0 H_0 + \mu_0 M_{eff})}$, where γ is the gyromagnetic ratio, $\mu_0 H_0$ is the resonance field and $\mu_0 M_{eff}$ is the effective diamagnetic field, will result in a d.c. voltage V_{dc} that is generated from the oscillating anisotropic magnetoresistance and spin-Hall magnetoresistance of the $Co_{40}Fe_{40}B_{20}$ layer. The RF power was fixed at 15 dBm (the RF power dependence is discussed further in Supplementary Information Note 2). We extracted the magnitude of the spin-Hall angle by performing Lorentzian function fitting, which was composed of symmetric L_S and antisymmetric L_A peaks representing spin–orbit torques and Oersted field torques, respectively. This can be described as $V_{dc} = V_S L_S(H) + V_A L_A(H)$, where $L_S(H) = \frac{w^2}{w^2+(H_{ext}+H)^2}$, $L_A(H) = \frac{w(H-H_0)}{w^2+(H-H_0)^2}$ and w is the resonance linewidth. With the above equations, we obtained $\theta_{SH} = \frac{J_S}{J_C} = (V_S/V_A)(e\mu_0 M_S t d/\hbar)\sqrt{(1+(M_{eff}/H_{ext})}$, where J_S is the spin-current density, J_C is the charge-current density, e is the elementary charge, μ_0 is vacuum permeability, M_S is the saturation magnetization of the magnetic layer, t is the effective thickness of the magnetic layer and d is the thickness of the non-magnetic layer. The saturation magnetization M_S of samples was measured by vibrating sample magnetometry and the effective thickness was estimated by a series-thickness dependent M_S of the $Co_{40}Fe_{40}B_{20}$ layer. Figure 2a shows a typical ST-FMR spectrum for our 6.6-nm composite-W sample at the f of I_{RF} 8 GHz along with the symmetric (red) and asymmetric (blue) components of the data extracted from the fitting. The damping constant was extracted by the frequency dependence linewidth expressed as $w = w_0 + \frac{2\pi f\alpha}{\gamma}$, where the frequency independent parameter w_0 represents the resonance peak broadening resulting from the inhomogeneity of materials. The typical spectrum is shown in Fig. 2b. To maximize the charge current that can be used for charge–spin conversion, the resistivity of spin–orbit coupling material is another important parameter to optimize owing to the shunting current running through the free layer, which, in our case, is the $Co_{40}Fe_{40}B_{20}$ layer. Considering both resistivity and spin-Hall angle, we used spin-Hall conductivity $\sigma_S = \theta_{SH}/\rho_{SOC}$ as the figure of merit to benchmark the performance of spin–orbit coupling material, where ρ_{soc} is the resistivity of spin–orbit coupling material (the corresponding spin-Hall angles and resistivity can be found in Supplementary Information Note 3). In our samples, the typical resistivity of the $Co_{40}Fe_{40}B_{20}$ layer and the 6.6-nm

https://doi.org/10.1038/s41928-025-01434-x

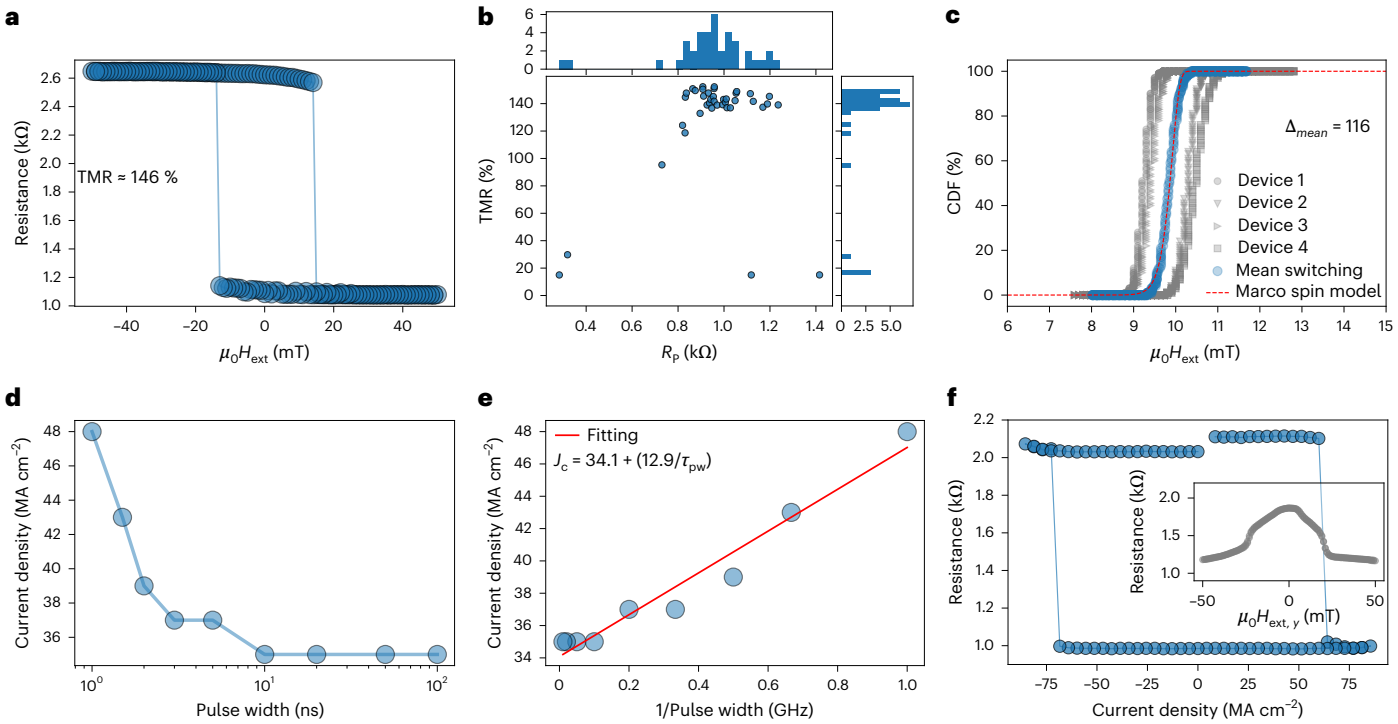

Fig. 4 | Device switching characterization. a, Magnetoresistance switching induced by a magnetic field applied in the *y* direction ($\mu_0 H_{ext}$) for the complete MTJ integrated on a 6.6-nm composite-W layer, with a TMR of approximately 146%. **b**, TMR versus parallel resistance state (R_P) of Type-Y cells and the corresponding histogram. **c**, CDF of switching as a function of the applied field, used for device retention extraction. Measurements were performed on four different devices from the same fabrication batch. The blue dots show the averaged CDF across the four devices fitted to the macro spin model (red dashed line). **d**, Pulse-width dependence of switching current density measured from 100 ns to 1 ns. **e**, Pulse-width dependence of critical current density J_c for SOT switching driven by the 6.6-nm composite-W spin–orbit coupling layer design (red line shows fit to the data). Each data point represents the mean value from measurements on 8,000 MTJs within the 64-kb SOT-MRAM chip. **f**, Type-X magnetoresistance switching induced by the applied current for the complete MTJ junction integrated on the 6.6-nm composite-W layer, demonstrating field-free switching. The inset shows magnetoresistance switching induced by a magnetic field applied in the *y* direction ($\mu_0 H_{ext,y}$).

composite-W layer were around 130 and 135 μΩ cm, respectively (micro-sized Hall bars of various $Co_{40}Fe_{40}B_{20}$ thicknesses were measured). Figure 2c shows the spin-Hall conductivity versus the thickness of the Co insertion layers. We found an optimal insertion layer thickness of about 0.14 nm, which is less than a monolayer of cobalt and hence the insertion layer is discontinuous in the Co-W composite structure. Supplementary Figs. 4 and 5 show the benchmarking of the ST-FMR extracted spin-Hall angle and spin-Hall conductivity (~4,500 Ω^{-1} cm^{-1}) of the composite-W, respectively. The intermixing effect between Co and W could be a reason why the inserted Co layer impedes the formation of α-W as this could consume the thermal budget, leading to a delayed transformation of the W. Data on further combinations of insertion layer thickness, materials and tungsten thickness can be found in Supplementary Fig. 6. Similar phase stability improvements were observed through introducing defects such as oxygen or nitrogen during the deposition of W[23–25,27–29]. In the process of increasing the spin-Hall conductivity, we took care not to negatively affect the damping constant, which is directly proportional to the critical switching current for type-Y SOT (Fig. 2d). We achieved a damping constant of around 0.007, which is an indicator that we fabricated good quality $Co_{40}Fe_{40}B_{20}$ layers and interfaces. The extracted demagnetization field as a function of Co-insertion thickness is shown in Fig. 2e. This decreasing trend of the demagnetization (from ~1.6 T to ~1.2 T) with decreasing Co thickness suggests that the interfacial energy between the $Co_{40}Fe_{40}B_{20}$ layer and the composite-W layer is enhanced by reducing the Co thickness. The reduced $\mu_0 M_{eff}$ also resulted in a lower switching current.

Harmonic Hall resistance measurements

In addition to the ST-FMR measurements, we conducted harmonic Hall resistance measurements for our 6.6-nm composite-W samples (Fig. 3). We patterned the samples into Hall bars (Fig. 3a) and applied an alternating current I_ω along the *x* direction. The device dimensions were 165 μm × 10 μm (inset in Fig. 3a). The in-phase first-harmonic V_ω and the out-of-phase second-harmonic voltages $V_{2\omega}$ were measured by using two lock-in amplifiers with the frequency of $\omega/2\pi$ = 191 Hz under the in-plane magnetic field applied to alter the moment *m* of the $Co_{40}Fe_{40}B_{20}$ layer (the angle between *m* and I_ω is defined as ϕ shown in Fig. 3a). Conventional spin–orbit torque is responsible for the damping-like torque parallel to $m \times (m \times \sigma_y)$ and the field-like torque along $m \times \sigma_y$, where σ_y is the *y* direction spin generated from the spin-Hall effect. The first-harmonic and second-harmonic Hall resistance can be expressed as[30]

$$R_{1\omega}^{xy} = R_P \sin 2\varnothing$$

and

$$R_{2\omega}^{xy} = \left(\frac{1}{2} R_A \frac{H_{DL}^{y}}{H_{ext} - H_k} + I_0 \alpha \nabla T\right) \cos\varnothing + \left(R_P \frac{H_{FL}^{y} + H_{Oe}}{H_{ext}}\right) \cos 2\varnothing \cos\varnothing + \frac{1}{2} R_A \frac{H_{DL}^{z}}{H_{ext} - H_k} \sin\varnothing + R_P \frac{H_{DL}^{z}}{H_{ext}} \cos 2\varphi + R_P \frac{H_{FL}^{x}}{H_{ext}} \cos 2\varnothing \sin\varnothing,$$

where R_P and R_A are the resistance changes originating from the planar Hall effect and the anomalous Hall effect, respectively. H_{DL}^{y} (H_{FL}^{y}) is the

Table 1 | SOT-MRAM performance benchmarking

	This work	TSRI 2023IEDM[34]	Tohoku 2019IEDM[35]	Intel 2020VLSI[36]	Imec 2021PRA[24]	Imec 2019VLSI[14]
Type	Y	Z (STT+SOT)	Canted X	Z (STT+SOT)	Z (Bx = 23 mT)	Z (Magnetic hard mask)
Design rule	Yes	Yes	No	Yes	Yes	Yes
Resilience to thermal budget (temperature)	400 °C	400 °C	400 °C	390 °C	300 °C	300 °C
Resilience to thermal budget (time)	10 h	30 min	NA	NA	30 min	NA
Integration with CMOS	Yes (64 kb array)	No	Yes	No	No	No
Spin-Hall angle	−0.61	−0.25	−0.37	−0.25	−0.42	−0.32
W resistivity (μΩ cm)	142	200	289	NA	150	160
Δ	116	62	70	NA	47	48
TMR (%)	145	130	140 (single device 167)	127	81	110
Switching efficiency (Δ/J_0, switching time=10 ns)	3.4	0.84	7.44	NA	NA	0.46
Switching efficiency (Δ/J_C, switching time=1 ns)	2.42	NA	2.97	NA	NA	0.37
Critical current density, J_C measured at 1 ns (MA cm^{-2})	48.0	NA	23.6	NA	~465 μA (J is not shown in the paper)	113 (290 μA)
J_C measured at 10 ns (MA cm^{-2})	34.1	74	9.4	15(SOT) + 2(STT)	~350 μA (J is not shown in the paper)	105

Summary of SOT-MRAM performances metrics. Design rules at advanced technology nodes explicitly define feature alignment and spacing requirements, which are more easily satisfied using vertical and horizontal patterns. This is particularly critical for maintaining precision in the front-end-of-line and BEOL layers. Failure to adhere to these design rules can affect yield and performance. Violating critical area rules amplifies the likelihood of defects during manufacturing, which reduces the yield of functional chips. In addition, non-compliant patterns are more susceptible to process variations, leading to inconsistent device performance or complete failures across the wafer. The switching efficiency is defined as Δ/J_C where Δ is the thermal stability and J_C is the critical current.

damping-like (field-like) field resulting from σ_y, H_k is the anisotropy field of the patterned device and H_{Oe} is the Oersted field generated from I_{RF}. The term of $I_0\alpha\nabla T$ is the harmonic Hall resistance change induced by thermoelectric effects including the anomalous Nernst effect and spin-Seebeck effect, which has no magnetic field dependency, where s the thermoelectric coefficient and ∇T is the thermal gradient along the z direction. The damping-like field originating from σ_x (σ_z) is denoted by H_{DL}^x (H_{DL}^z) and H_{FL}^x is the field-like field from σ_x. Further details on the unconventional spin component extracted from harmonic measurements are provided in Supplementary Information Note 1, including Supplementary Figs. 7 and 8 and Supplementary Table 1.

From the above equations, we were able to decompose the spin–orbit torque exerted on the ferromagnetic moments into three directions, x, y and z, as well as exclude the thermoelectric effect by conducting an in-plane magnetic field ∅ sweep (Fig. 3b,c). The R_p of the device was 237 mΩ by the fitting result shown in Fig. 3b. Figure 3c,d shows the ∅ dependence of $R_{1\omega}^{xy}$ and $R_{2\omega}^{xy}$ of the device fabricated on the 6.6-nm composite-W sample under $\mu_0 H_{ext}$ = 0.155 T. The representative measured $R_{2\omega}^{xy}$ (blue dots) is plotted in Fig. 3c and fitted with the corresponding equation above (dash lines). We can see that the data is well fitted with mainly the H_{DL}^y term, which has cos ∅ dependence, and partially with H_{FL}^y. To quantify the magnitude of H_{DL}^y and H_{FL}^y, we conducted $\mu_0 H_{ext}$ dependence measurements ranging from 27.7 mT to 210 mT shown in Fig. 3d (preventing the nonlinear response at the small field). From the field dependence data, we could extract all the fitted terms and calculate the damping (field)-like torque efficiency originated from the conventional spin-Hall effect components (y) using $\xi_{DL}^y = \frac{2e}{\hbar}\frac{H_{DL}M_S t}{j_{W-Co}}$ and $\xi^y = \frac{2e}{\hbar}\frac{H_{FL}M_S t}{j_{W-Co}}$, where $j_{W\text{-}Co}$ is the current density running through the W-Co layer. The damping-like torque efficiency was ~0.61, which is consistent with the θ_{SH} measured from ST-FMR (0.56) for the negligible field-like torque.

Device characterization

To evaluate the SOT switching performance, we implemented a 64-kb Type-Y SOT-MRAM fabrication flow based on the composite-W film scheme. Type-Y SOT-MRAM offers several advantages over Type-Z (p-MTJ). Detailed comparison of Type-Y, Type-X and Type-Z geometries is provided in Supplementary Information Note 2 and Supplementary Figs. 9–12, including good energy efficiency in the sub-10-ns regime and reliability (Supplementary Fig. 12), making it a more appealing solution for high-speed and low-power memory applications[31]. The details of 64 kb SOT-MRAM can be found in Supplementary Fig. 13 (see Methods for process details). Figure 4a shows the typical tunnelling magnetoresistance (TMR) value (around 146%) measured from the SOT test kit (set-up is shown in Supplementary Fig. 14), confirming the excellent interface quality between MgO and $Co_{40}Fe_{40}B_{20}$. This high TMR ensures a sufficient read margin and a robust process window, facilitating future scaling-up efforts. Figure 4b, a histogram of the TMR ratio versus resistance R_p collected from 40 different devices on the SOT test kit, shows the device-to-device variation (set-up is shown in Supplementary Fig. 14).

In addition, we estimated the thermal stability (Δ) and anisotropy field (H_k) of the free layer using the cumulative distribution function (CDF) with macro spin model[32,33]

$$\mathrm{CDF} = 1 - \exp(f_0 H_k/2R\sqrt{\pi/\Delta}(\mathrm{erf}\left(\sqrt{\Delta}\,(1 - H/H_k)\right) - \mathrm{erf}(\sqrt{\Delta}))),$$

where f_0 is the attempt frequency taken as 1 GHz, H is the given applied field and R is the field ramp rate (15 Hz for the case shown in Fig. 4c). The mean value of Δ, extracted from Fig. 4c, was approximately 116 at room temperature. This high thermal stability is advantageous for scaling down switching currents in ultralow-power embedded memory applications, as it enables the reduction of magnetic volume in the free layer. Figure 4d shows the pulse-width-dependent switching behaviour

of the MTJ driven by CMOS (the pulse generation details are provided in Methods) measured from 8,000 devices on the 64 kb SOT-MRAM chip. Figure 4e shows current density J_C versus the reciprocal number of applied pulsed width ($1/\tau_{pw}$), where we define J_C as the average current density to drive the resistance of MTJ from parallel (R_P) to antiparallel (R_{AP}) and R_{AP} to R_P. We used the expression $J_C = J_0 + q/\tau_{pw}$ [20], where J_0 is the intrinsic switching current density for the long pulse (10 ns in our case), to fit the data shown in Fig. 4e. From the fitting result, we obtained $J_0 = 34.1$ MA cm^{-2} and $q = 12.9$ kC cm^{-2}, providing insights into the switching characteristics of the device. To assess the competitiveness of our composite-W-based SOT-MRAM, we benchmarked our devices against state-of-the-art reports (summarized in Table 1). The comparison highlights that our composite-W design offers the most manufacturable and energy-efficient solution for embedded MRAM, ensuring scalability, reliability and compliance with CMOS fabrication constraints. Finally, we demonstrate field-free Type-X switching (Fig. 4f) measured on the SOT test kit set-up due to the symmetry-breaking properties of composite-W (Fig. 1c and Supplementary Information Note 1). The inset of Fig. 4f shows the hard-axis behaviour of the TMR when an external field is applied along the y axis, which confirms that shape anisotropy favours magnetization alignment along the x direction.

Conclusions

We have reported a Co insertion layer design that can be used to stabilize the β-W phase under a BEOL thermal budget. Our β-W films exhibit a spin-Hall conductivity of approximately 4,500 Ω^{-1}cm^{-1}. Using ST-FMR and harmonic Hall resistance measurements on the composite-W, we provide insights into the spin-Hall conductivity, Gilbert damping constant and effective magnetization. Furthermore, we used the composite-W film stack to create a 64-kb SOT-MRAM that offers 1 ns SOT switching with a 146% TMR and data retention greater than 10 years (Δ of around 116). Our approach could be of use in the development of high-speed and low-power MRAM applications.

Methods

Sample growth and thin-film characterization

The W-MTJ films were deposited on SiO_x substrates using magnetron physical vapour deposition under high vacuum conditions (base pressure $<5 \times 10^{-9}$ T) and a working pressure of 5×10^{-3} T with an argon flow rate of 40 sccm at the MRAM facilities at Electronic and Optoelectronic System Research Laboratories, Industrial Technology Research Institute, Hsinchu, Taiwan. During deposition, d.c. power was applied to the W target, and substrate rotation at 60 rpm ensured film uniformity. The deposition process was carried out at room temperature. Following deposition, the films underwent annealing to optimize the β-W to α-W phase transition, enhancing the crystalline structure.

Thin sections for TEM were prepared by a focused ion beam in an FEI Helios Nanolab 660 TEM analysis was carried out with a Hitachi HF-5000 equipped with a probe aberration corrector, under 200 kV. Bright field, secondary electron and annular (both medium- and high-angle) dark-field images were captured simultaneously in scanning TEM mode. High-resolution energy-dispersive X-ray spectroscopy mapping and line scans were performed with an Oxford Instruments large solid angle (2.0 sr) dual windowless detector supported by Taiwan Semiconductor Manufacturing Company (TSMC).

Nanodiffraction

The crystal structure and orientation distribution of W films were identified through synchrotron-based nanodiffraction techniques at the Taiwan Photon Source (TPS) beamline 21 A at the National Synchrotron Radiation Research Center (NSRRC). Before the measurements, an online real-time FESEM instrument as a navigator was used to position the observed regions. A spot of size 90×90 nm^2 using monochromatic X-rays was focused on the same areas as in FESEM to collect the spatial diffraction maps of W films. To better collect the diffraction signal for different W phases, wavelengths of 1.6316 Å and 1.5215 Å were adopted to measure the composite-W and single-layer-W films, respectively.

Device fabrication and electrical characterization

The processes involved in preparing the thin films for magnetotransport, Hall harmonic voltage and magnetization switching experiments included patterning them into Hall bars using optical lithography and e-beam lithography for MTJ devices. These Hall bars used in the experiments had width 10 μm and length 165 μm, with a separation of 28 μm between the Hall crosses within the device. For ST-FMR measurements, the thin films were patterned into rectangular strips measuring 20 μm in width and 60 μm in length.

The Type-Y (-X) MTJ had lateral dimensions of 75 nm × 230 nm (230 nm × 75 nm). Type-X rotated the long axis of the MTJ by 90° relative to Type-Y. The fabrication process, composite-W integration and characterization procedures remain identical. The full layer stack, from top to bottom, consisted of a pinning layer (PtMn, 10–20 nm), a synthetic antiferromagnetic layer (Co/Ru/Co), a reference layer ($Co_{0.2}Fe_{0.6}B_{0.2}$, 2.0–2.9 nm), a tunnelling barrier (MgO, 1.2 nm), a free layer ($Co_{0.2}Fe_{0.6}B_{0.2}$, 1.2–2.9 nm) and a spin-current source layer of composite-W.

Following the initial photolithography step, a precision argon ion mill was employed to precisely define the device geometry. Subsequently, Ti (10 nm)/Au (120 nm) thick electrical contacts were deposited after the second lithography step using a KJL e-beam evaporator.

For voltage and current measurements, two lock-in amplifiers SR-830 and a Keithley 6221 current source were used to probe the first- and second-harmonic Hall voltage and supply current with a frequency of 191 Hz, respectively. In addition, an Agilent HP 83620B served to supply RF current for the ST-FMR measurements, whereas the d.c. voltage was measured with a Keithley 2000 voltagemeter. ST-FMR and Hall voltage measurements were conducted on coupon samples.

For the pulse-width-dependent switching measurements, two distinct pulse waveforms were applied through an XOR gate to generate a differential pulse. The shortest pulse that could be generated was 1 ns. The switching behaviour presented in Fig. 4d,e was measured on the 64-kb SOT-MRAM chip, based on the statistical evaluation of 8,000 MTJs.

Test kit and 64-kb SOT-MRAM device layout

The 64-kb SOT-MRAM test chip was fabricated using a Type-Y configuration with a total of $64 \times 64 = 4{,}096$ bit-cells per array. Each test chip included two identical SOT-MRAM arrays (8,192 cells in total) embedded within an IO function block (Supplementary Fig. 13). Each bit-cell consisted of a three-terminal structure integrating a composite-W spin-Hall channel and a CoFeB/MgO/CoFeB MTJ stack.

The layout featured 26 write word lines and 26 read word lines, along with 26 write bit lines, 26 read bit lines and 26 source lines for the SOT current path. Bit-cells were selectively addressed using a local decoder architecture and accessed by means of multiplexers and sense amplifiers positioned per column.

The MTJs had elliptical shapes with dimensions of 75 nm × 230 nm for Type-Y and 230 nm × 75 nm for Type-X configurations. The composite-W layer in each cell consisted of four W/Co stacks (W 1.65 nm/Co 0.14 nm × 4) to stabilize the β-W phase under BEOL thermal budgets. The full layer stack from bottom to top was Si/SiO_2/composite-W/$Co_{40}Fe_{40}B_{20}$ (2.0 nm)/MgO (1.5 nm)/$Co_{40}Fe_{40}B_{20}$ (2.0–2.9 nm)/synthetic antiferromagnet (Co/Ru/Co)/PtMn (10–20 nm).

Characterization was conducted using a custom-designed SOT test-kit structure (Supplementary Fig. 13) to measure TMR, critical current density and switching speed. The metal routing provided direct access to the MTJ's top electrode and four separate bottom electrodes (BE1S, BE2S, BE1G, BE2G), enabling both two-terminal and three-terminal probing configurations.

Switching behaviour under nanosecond pulses was evaluated by applying XOR-generated differential pulses, with the shortest pulse duration reaching 1 ns. The data presented in Fig. 4d,e are based on measurements across 8,000 bit-cells.

Data availability

The data that support the findings of this study are available from the corresponding author upon reasonable request. Access to the data may be subject to a data use agreement in compliance with applicable legal and ethical requirements.

Code availability

Codes to perform signal fitting and micromagnetic simulation are available from the corresponding authors upon reasonable request.

References

1. Makarov, A., Sverdlov, V. & Selberherr, S. Emerging memory technologies: trends, challenges, and modeling methods. *Microelectron. Reliab.* **52**, 628–634 (2012).
2. Yu, S. & Chen, P.-Y. Emerging memory technologies: recent trends and prospects. *IEEE Solid-State Circuits Mag.* **8**, 43–56 (2016).
3. Wong, H.-S. P. et al. Phase change memory. *Proc. IEEE* **98**, 2201–2227 (2010).
4. Qureshi, M. K., Srinivasan, V. & Rivers, J. A. Scalable high performance main memory system using phase-change memory technology. In *Proc. of the 36th Annual International Symposium on Computer Architecture* 24–33 (ACM, 2009).
5. Mikolajick, T.,Slesazeck, S., Park, M. H. & Schroeder, U. Ferroelectric hafnium oxide for ferroelectric random-access memories and ferroelectric field-effect transistors. *MRS Bull.* **43**, 340–346 (2018).
6. Sheikholeslami, A. & Gulak, P. G. A survey of circuit innovations in ferroelectric random-access memories. *Proc. IEEE* **88**, 667–689 (2000).
7. Wong, H.-S. P. & Salahuddin, S. Memory leads the way to better computing. *Nat. Nanotechnol.* **10**, 191–194 (2015).
8. Sebastian, A., Le Gallo, M., Khaddam-Aljameh, R. & Eleftheriou, E. Memory devices and applications for in-memory computing. *Nat. Nanotechnol.* **15**, 529–544 (2020).
9. Roy, K., Jaiswal, A. & Panda, P. Towards spike-based machine intelligence with neuromorphic computing. *Nature* **575**, 607–617 (2019).
10. Ielmini, D. & Wong, H.-S. P. In-memory computing with resistive switching devices. *Nat. Electron.* **1**, 333–343 (2018).
11. Zhang, W., Mazzarello, R., Wuttig, M. & Ma, E. Designing crystallization in phase-change materials for universal memory and neuro-inspired computing. *Nat. Rev. Mater.* **4**, 150–168 (2019).
12. Guo, Z. et al. Spintronics for energy-efficient computing: an overview and outlook. *Proc. IEEE* **109**, 1398–1417 (2021).
13. Sun, Z. et al. A full spectrum of computing-in-memory technologies. *Nat. Electron.* **6**, 823–835 (2023).
14. Garello, K. et al. Manufacturable 300mm platform solution for field-free switching SOT-MRAM. In *2019 Symposium on VLSI Circuits* T194–T195 (IEEE, 2019).
15. Couet, S. et al. BEOL compatible high retention perpendicular SOT-MRAM device for SRAM replacement and machine learning. In *2021 Symposium on VLSI Technology* 1–2 (IEEE, 2021).
16. Song, M. et al. High speed (1ns) and low voltage (1.5 V) demonstration of 8Kb SOT-MRAM array. In *2022 IEEE Symposium on VLSI Technology and Circuits (VLSI Technology and Circuits)* 377–378 (IEEE, 2022).
17. Grimaldi, E. et al. Single-shot dynamics of spin–orbit torque and spin transfer torque switching in three-terminal magnetic tunnel junctions. *Nat. Nanotechnol.* **15**, 111–117 (2020).
18. Gupta, M. et al. High-density SOT-MRAM technology and design specifications for the embedded domain at 5nm node. In *2020 IEEE International Electron Devices Meeting (IEDM)* 24.25. 21–24.25. 24 (IEEE, 2020).
19. Fukami, S., Anekawa, T., Ohkawara, A., Zhang, C. & Ohno, H. A sub-ns three-terminal spin-orbit torque induced switching device. In *2016 IEEE Symposium on VLSI Technology* 1–2 (IEEE, 2016).
20. Garello, K. et al. Ultrafast magnetization switching by spin-orbit torques. *Appl. Phys. Lett.* **105**, 212402 (2014).
21. Endoh, T., Honjo, H., Nishioka, K. & Ikeda, S. Recent progresses in STT-MRAM and SOT-MRAM for next generation MRAM. In *2020 IEEE Symposium on VLSI Technology* 1–2 (IEEE, 2020).
22. Pai, C.-F. et al. Spin transfer torque devices utilizing the giant spin Hall effect of tungsten. *Appl. Phys. Lett.* **101**, 122404 (2012).
23. Demasius, K.-U. et al. Enhanced spin–orbit torques by oxygen incorporation in tungsten films. *Nat. Commun.* **7**, 10644 (2016).
24. Vudya Sethu, K. K. et al. Optimization of tungsten β-phase window for spin-orbit-torque magnetic random-access memory. *Phys. Rev. Appl.* **16**, 064009 (2021).
25. Takeuchi, Y. et al. Spin-orbit torques in high-resistivity-W/CoFeB/MgO. *Appl. Phys. Lett.* **112**, 192408 (2018).
26. Rahaman, S. Z. et al. Pulse-width and temperature effect on the switching behavior of an etch-stop-on-MgO-barrier spin-orbit torque MRAM cell. *IEEE Electron Device Lett.* **39**, 1306–1309 (2018).
27. O'keefe, M. & Grant, J. Phase transformation of sputter deposited tungsten thin films with A-15 structure. *J. Appl. Phys.* **79**, 9134–9141 (1996).
28. Shen, Y. & Mai, Y. Influences of oxygen on the formation and stability of A15 β-W thin films. *Mater. Sci. Eng. A* **284**, 176–183 (2000).
29. Chattaraj, A. et al. Unravelling oxygen driven α to β phase transformation in tungsten. *Sci. Rep.* **10**, 14718 (2020).
30. Avci, C. O. et al. Interplay of spin-orbit torque and thermoelectric effects in ferromagnet/normal-metal bilayers. *Phys. Rev. B* **90**, 224427 (2014).
31. Fukami, S., Anekawa, T., Zhang, C. & Ohno, H. A spin–orbit torque switching scheme with collinear magnetic easy axis and current configuration. *Nat. Nanotechnol.* **11**, 621–625 (2016).
32. Feng, X. & Visscher, P. Sweep-rate-dependent coercivity simulation of FePt particle arrays. *J. Appl. Phys.* **95**, 7043–7045 (2004).
33. Van Beek, S. et al. Thermal stability analysis and modelling of advanced perpendicular magnetic tunnel junctions. *AIP Adv.* **8**, 055909 (2018).
34. Li, K.-S. et al. First BEOL-compatible, 10 ns-fast, and Durable 55 nm Top-pSOT-MRAM with High TMR (130%). In *2023 International Electron Devices Meeting (IEDM)* 1–4 (IEEE, 2023).
35. Honjo, H. et al. First demonstration of field-free SOT-MRAM with 0.35 ns write speed and 70 thermal stability under 400° C thermal tolerance by canted SOT structure and its advanced patterning/SOT channel technology. In *2019 IEEE International Electron Devices Meeting (IEDM)* 28.25. 21–28.25. 24 (IEEE, 2019).
36. Sato, N. et al. CMOS compatible process integration of SOT-MRAM with heavy-metal bi-layer bottom electrode and 10ns field-free SOT switching with STT assist. In *2020 IEEE Symposium on VLSI Technology* 1–2 (IEEE, 2020).

Acknowledgements

We acknowledge S.-J. Lin, who initiated this project and engaged in constructive discussions at TSMC. We also acknowledge C. Diaz, J. Sun and C.-F. Pai for fruitful discussions. Y.-L.H. acknowledges financial support from the Center for Semiconductor Technology Research from the Featured Areas Research Center Program within the framework of the Higher Education Sprout Project by the Ministry of Education in Taiwan, and from the National Science and Technology

Council, Taiwan, under grant nos. NSTC 110-2634-F-009-027, NSTC 111-2112-M-A49-012-MY3 and NSTC 113-2112-M-A49-029-. Y.-L.H. also acknowledges the Center for Emergent Functional Matter Science of National Yang Ming Chiao Tung University from The Featured Areas Research Center Program within the framework of the Higher Education Sprout Project by the Ministry of Education in Taiwan. S.X.W. and F.X. acknowledge that their work at Stanford was supported in part by Precourt Institute for Energy and the SystemX Alliance at Stanford, under NSF grant nos. 2314591 (ACED Fab) and 2328804 (FuSe), and by the SRC GRC Program. Part of this work was performed at the Stanford Nanofabrication Facility (SNF) and Stanford Nano Shared Facilities (SNSF), supported by the National Science Foundation under award ECCS-2026822. We acknowledge the assistance and beam time provided by the Taiwan Photon Source (TPS) 21A X-ray Nanodiffraction beamline at the National Synchrotron Radiation Research Center (NSRRC).

Author contributions

Y.L.H. supervised the project and wrote the manuscript with input from all authors. Y.L.H. also designed the film stack, performed device fabrication, spin-Hall conductivity measurements and micromagnetic simulations. M.Y.S., C.M.L., G.L.C., S.Y.Y., Y.J.C., I.J.W., Y.C.H., Y.H.S. and J.H.W. were responsible for CMOS-based MTJ integration and device characterization. Y.W.C. and S.H.C. conducted the time- and temperature-dependent annealing experiments and GIXRD analysis. L.C.H. and F.X. contributed to partial device fabrication. C.Y.C. and H.J.L. performed X-ray nanodiffraction measurements. All authors actively discussed the results, contributed to data interpretation and provided feedback throughout the experimental and analytical process.

Competing interests

The authors declare no competing interests.

Additional information

Supplementary information The online version contains supplementary material available at https://doi.org/10.1038/s41928-025-01434-x.

Correspondence and requests for materials should be addressed to Yen-Lin Huang.

Peer review information *Nature Electronics* thanks Byong-Guk Park and the other, anonymous, reviewer(s) for their contribution to the peer review of this work.

Reprints and permissions information is available at www.nature.com/reprints.

Publisher's note Springer Nature remains neutral with regard to jurisdictional claims in published maps and institutional affiliations.

Springer Nature or its licensor (e.g. a society or other partner) holds exclusive rights to this article under a publishing agreement with the author(s) or other rightsholder(s); author self-archiving of the accepted manuscript version of this article is solely governed by the terms of such publishing agreement and applicable law.

© The Author(s), under exclusive licence to Springer Nature Limited 2025